Çukurova Üniversitesi
Mühendislik Fakültesi Dergisi
Çukurova University
Journal of the Faculty of Engineering
ISSN: 2757-9255 CİLT/VOLUME: 41 SAYI/ISSUE: 3 EYLÜL/SEPTEMBER 2026

Assessment of the Eddy Viscosity-Based Turbulence Models on the Solution of the Highly Separated/Attached Flow

Ahmet Remzi ERKOÇ [1,a], **Tural TUNAY** [1,b]

[1]*Adana Alparslan Türkeş Science and Technology University, Faculty of Engineering, Department of Mechanical Engineering, Adana, Türkiye*

[a]***ORCID***: *0009-0002-9308-7418;* [b]***ORCID***: *0000-0001-5994-4565*

Article Info
Received : 09.06.2026
Accepted : 25.09.2026
DOI: 10.21605/cukurovaumfd.1966832

Corresponding Author
Tural TUNAY
ttunay@atu.edu.tr

Keywords
Backward facing step (BFS)
Reattachment length
Separated and reattached flow
Turbulence models

How to cite: *ERKOÇ, A.R., TUNAY, T., (2026). Assessment of the Eddy Viscosity-Based Turbulence Models on the Solution of the Highly Separated/Attached Flow. Cukurova University, Journal of the Faculty of Engineering, 41(3), 747-760.*

ABSTRACT

The present study investigated performance of different turbulence models based on the Reynolds-averaged Navier-Stokes (RANS) equations to solve the flow over a backward-facing step (BFS). Three different turbulence models, i.e., Spalart-Allmaras, Realizable k-ε and SST k-ω turbulence models, were investigated for the flow over BFS. The investigations were performed for the Reynolds number of $Re_h = 9.6 \times 10^3$ based on step height, h, and the free stream velocity, U_∞. The results, which are validated against the experimental data, showed that the Spalart–Allmaras model predicted the reattachment length, X_r, with an error of 9.52%. The Realizable k-ε and SST k–ω models overpredicted the reattachment length, X_r, by 26.7% and 38.1%, respectively. Within the recirculation region, however, the SST k-ω provided the best prediction of the streamwise velocity, with a maximum difference of 5% from the experimental measurements. The largest local difference of 191% was obtained with the Spalart–Allmaras model at $x/h = 1$.

Yüksek Derecede Ayrılmış/Bağlı Akışın Çözümünde Girdap Viskozitesi Tabanlı Türbülans Modellerinin Değerlendirilmesi

Makale Bilgileri
Geliş : 09.06.2026
Kabul : 25.09.2026
DOI: 10.21605/cukurovaumfd.1966832

Sorumlu Yazar
Tural TUNAY
ttunay@atu.edu.tr

Anahtar Kelimeler
Geri adımlı yüzey
Yeniden bağlanma uzunluğu
Ayrılmış ve yeniden bağlanmış akış
Türbülans modelleri

Atıf şekli: *ERKOÇ, A.R., TUNAY, T., (2026). Yüksek Derecede Ayrılmış/Bağlı Akışın Çözümünde Girdap Viskozitesi Tabanlı Türbülans Modellerinin Değerlendirilmesi. Çukurova Üniversitesi, Mühendislik Fakültesi Dergisi, 41(3), 747-760.*

ÖZ

Bu çalışmada, geri adımlı yüzey (Backward Facing Step, BFS) üzerindeki akışı çözmek için Reynolds Ortalamalı Navier-Stokes (RANS) denklemlerine dayanan farklı türbülans modellerinin performansı araştırılmıştır. BFS üzerindeki akışın çözümünde Spalart-Allmaras, Realizable k-ε ve SST k-ω olmak üzere üç farklı türbülans modeli incelenmiştir. Araştırmalar, serbest akım hızı, U_∞ ve basamak yüksekliği, h baz alınarak tanımlanan $Re_h = 9.6 \times 10^3$ Reynolds sayısı için gerçekleştirilmiştir. Deneysel verilerle doğrulanan sonuçlar, Spalart-Allmaras modelinin yeniden bağlanma uzunluğunu, X_r, 9.52%'lik bir hata ile tahmin ettiğini göstermiştir. Realizable k-ε ve SST k-ω modelleri yeniden bağlanma uzunluğunu, X_r, sırasıyla %26.7 ve %38.1 oranında fazla tahmin etmiştir. Bununla birlikte, geri akış bölgesinde, SST k-ω modeli akış yönündeki hız bileşenini deneysel ölçümlerden maksimum 5%'lik bir farkla en iyi şekilde tahmin etmiştir. En büyük lokal fark olan %191, Spalart-Allmaras modeli ile x/h = 1 noktasında elde edilmiştir.

1. INTRODUCTION

A downstream wake region develops behind an object with its spatial extent governed by both the geometric properties of the object (e.g., bluff shapes, geometric discontinuities, or sudden expansions) and the flow features, such as boundary-layer separation. These wakes are characterized by interacting shear layers and recirculation zones that exhibit highly unsteady, three-dimensional turbulent behaviour. Wake flows of this nature are encountered in many engineering applications, which includes flow over airfoils, flow around ground vehicles, and flow through corrugated or patterned channels [1-4].

The flow over a backward-facing step (BFS) exhibits the fundamental characteristics of wake flows, including free shear layer separation, vortex development, and subsequent flow reattachment [5]**.** The flow over a BFS exhibits a strong adverse pressure gradient after separation [6]. It is followed by the formation of a large recirculation zone downstream of the step. Within this recirculation zone, strong velocity gradients, vortex shedding, and turbulence production occur, which leads to complex unsteady flow behaviour. Uruba et al. [1] examined that the reattachment of the flow downstream of the BFS is a highly non-stationary dynamical process, so that the zone of reattachment needs to be discussed rather than the point and the line when describing it. Previous studies showed that the length of the reattachment in the BFS flow depends on the Reynolds number (Re), step height (h), and the boundary layer thickness (δ) of the incoming flow [7]. Near the BFS, the pressure coefficient (C_p) and skin friction coefficient (C_f) decrease and subsequently increase gradually along the downstream flow [8]. A low-static-pressure region exists below the shear layer which causes part of the reattached flow to recirculate upstream and form a recirculation zone [9]. In a large part of that zone, the wall shear stress is assumed to be negative [8, 10, 11]. The skin friction coefficient was observed to decrease with increasing Reynolds number in the study of Tihon et al. [10].

In the numerical analysis of turbulent flows including wakes, the selection of an appropriate turbulence model plays a critical role in determining both the accuracy of the predictions and the associated computational cost. Advanced approaches, e.g., Large Eddy Simulation (LES), require highly refined grids and small-time steps to resolve a wide range of turbulent scales, which makes them computationally demanding and typically suitable only for high-performance computing environments. In contrast, turbulence models, based on the Reynolds-Averaged Navier–Stokes (RANS) equation, remain widely used in engineering applications because they offer a favourable balance between accuracy and efficiency [12]. RANS approaches can deliver reliable predictions while operating on significantly more modest computational systems by modelling the entire turbulence spectrum. Karabulut and Alnak [13] investigated the flat and triangular step pattern in channel flow by using RANS turbulence model that is k-ε turbulence model at different Re_h. The results showed that the Nusselt number (Nu) is increased by Reynolds number in both cases.

The BFS geometry is widely used to evaluate the performance of turbulence models in capturing wake flow characteristics [15]. Researchers often use the computational simulations and experimental data of flows over BFS to assess the accuracy and performance of turbulence models. Therefore, numerous studies in the literature have employed the BFS geometry to assess the performance of turbulence models [15-18].

Driver and Seegmiller [16] evaluated the performance of eddy-viscosity turbulence models, i.e., k-ε and algebraic-stress turbulence models (ASM), by comparing with their experimental data. The results showed that the modified ASM improved the results of the unmodified ASM and the k-ε model, while it overpredicts the dissipation rate. Additionally, Gatski et al. [17] found that the standard k-ε model predicts the reattachment point location with an 11% underestimation relative to the nonlinear k-ε model. The assumption of isotropic eddy viscosity in the standard k-ε model and its variants lead to inaccurate predictions of normal Reynolds stresses, which in turn results in errors in estimating the reattachment length [19]. Additionally, the standard k-ε model can produce unphysical results, including negative values of the turbulent kinetic energy (k) and the turbulent dissipation rate (ε).

The Realizable k-ε model was suggested by Shih et al. [20], which was designed to better capture the turbulence anisotropy by modifying the eddy viscosity formulation to provide more accurate predictions in flows such as near-wall flows and in separated flows. The Realizable k-ε model introduces improvements in the formulation of eddy viscosity along with additional constraints to ensure physically consistent

predictions of the turbulent kinetic energy (k) and dissipation rate (ε), thereby enhancing the realism and accuracy of turbulent flow simulations. Additionally, the Realizable k-ε model performs well in predicting complex flow features, including separation, reattachment, and recirculation, as observed in BFS flows. Accordingly, Shih et al. [20] reported that the Realizable k-ε model solved the reattachment length with an error less than 2% when compared with the experimental results of Driver and Seegmiller [16] for the case of a smaller step height.

Additionally, Wilcox [15] reported that the Spalart–Allmaras model predicts the reattachment point location within 3% of the experimental data obtained by Driver and Seegmiller [16]. Bredberg and Davidson [18] emphasized the importance of cross-diffusion terms in eliminating freestream sensitivity with respect to ω in free shear flows and proposed an improved k-ω turbulence model that does not require wall functions or wall-distance information. Furthermore, Munters et al. [21] compared various turbulence modelling approaches, including scale-resolving, Reynolds-averaged, and hybrid models, for flow over the BFS at a Reynolds number of $Re_h = 6.4\times10^3$ and an expansion ratio of $H_o/H_i = 2.25$. Their results indicated that DES and IDDES models, which incorporate wall-modelled LES, provide more accurate predictions, whereas SAS and DDES perform less satisfactorily. In particular, DDES was found to suffer from model-stress depletion (MSD), while SAS yielded results similar to those of RANS models.

Scale-resolving turbulence models, such as direct numerical simulation (DNS) and large eddy simulation (LES), which enable accurate stability analysis, have also been employed in the previous studies to investigate flow over the BFS [22-25]. Thus, the characteristics of the average flow over the BFS, which shows convective or absolute instability were revealed. These studies demonstrated that, in the absence of external disturbances, the flow over the BFS remains time-independent for Reynolds numbers $Re_h < 2500$. In contrast, the presence of external excitation can lead to time-dependent behaviour. For instance, under small-amplitude monochromatic excitation, the flow exhibits time-periodic behaviour when the excitation frequency is close to the shear-layer frequency, while it remains largely unaffected at higher excitation frequencies. When random noise is introduced, the flow becomes unsteady, characterized by a dominant frequency near that of the shear layer [24]. Furthermore, simulations at an expansion ratio of $H_o/H_i = 5$ revealed that the eddy structures exhibit strong similarities to those observed in forced plane mixing layers, with large-scale billows forming downstream of the step and intense longitudinal vortices developing between them [25].

Previous studies using turbulence models to solve the separated flow field downstream of BFS are summarised in Table 1. These studies showed that the prediction of BFS flow depends strongly on the turbulence model used while the correct prediction of the separated flow characteristics is a critical phenomenon influencing the aerodynamic performance and the rate of heat transfer [26]. As presented in Table 1, direct comparison among the findings of these previous studies is difficult because the studies differ in geometry and Reynolds number. Moreover, turbulence model performance has frequently been summarised using only the reattachment length, even though a turbulence model that predicts this global quantity accurately may not reproduce the local velocity field with comparable accuracy.

While scale-resolving approaches, such as LES and DES, can accurately capture the unsteady vortex dynamics and shear-layer instabilities inherent to BFS flows, their high computational cost limits their feasibility in many industrial applications. Consequently, RANS models remain the primary choice for engineering design, optimization, and routine CFD analyses. However, the predictive capability of these models remains strongly problem-dependent, particularly in flows involving separation, reattachment, and recirculation. Therefore, a comprehensive assessment of RANS turbulence models for BFS geometries is still required to clarify their strengths, limitations, and applicability ranges.

The present study investigated the performance of several eddy viscosity-based Reynolds-Averaged Navier–Stokes (RANS) turbulence models in predicting the flow characteristics over a BFS. Three turbulence models, i.e., Spalart–Allmaras, Realizable k-ε, and SST k-ω, were applied. Steady-state simulations were performed for all turbulence models at a Reynolds number of $Re_h = 9.6 \times 10^3$, which was defined based on the step height h and the free-stream velocity, U_∞ of the flow. The novelty of the present study lies in evaluating three widely used eddy-viscosity based RANS turbulence models (i.e.,

Spalart-Allmaras, Realizable k-ε and SST k-ω) under the same BFS geometry, Reynolds number and inflow boundary conditions. Additionally, the present study assesses the performance of the turbulence models using both global and local flow characteristics, e.g., the reattachment length, streamwise velocity profiles, the secondary recirculation flow structure, vorticity, skin-friction coefficient and pressure coefficient.

Table 1. Previous studies using turbulence models to solve the separated flow field downstream of BFS

Study	H_o/H_i	Re_h	Turbulence models	X_r/h
Present Work	1.08	9.6×10^3	Spalart-Allmaras, Realizable k-ε, SST k-ω	4.6 5.3 5.8
Addad et al. [27]	1.10	1.7×10^5	LES	4.0
Al-Jelawy et al. [11]	1.13	5.7×10^4	SST k-ω Spalart-Almaras	5.6 6.1
Khuwaranyu and Putivisutisak [28]	1.20	5.0×10^3	k-ω – LSC	6.3
Bredberg and Davidson [18]	1.20	5.1×10^3	Standard k-ω	6.3
Kang and Choi [29]	1.20	5.1×10^3	LES	6.2
Le et al. [22]	1.20	5.1×10^3	DNS	6.3
Okada et al. [30]	1.25	5.0×10^3	LES	5.9
Avancha and Pletcher [31]	1.50	5.5×10^3	LES	6.1
Dejoan and Leschziner [32]	1.50	3.7×10^3	LES	7.0
Rhee and Sung [33]	1.50	3.3×10^4	k-ε- f	7.3
Mehrez et al. [34]	1.50	3.3×10^4	LES	7.2
Choi and Kim [35]	1.50	4.8×10^4	Standard k-ε RNG NLEVM EARSM	5.9 6.2 6.9 7.4
Kumar et al. [36]	1.94	7.0×10^3 7.5×10^3 $8.0.\times 10^3$ 8.5×10^3 9.0×10^3	Standard k-ε	5.9 5.9 6.0 6.0 6.0
Barri and Andersson [37]	2.00	5.6×10^3	DNS	7.1
Louda et al. [38]	2.00	1.5×10^4	EARSM	8.5 8.2
Juste et al. [39]	2.00	0.2×10^3 0.3×10^3 0.5×10^3 0.7×10^3	LES	4.9 6.2 9.8 13.5
Munters et al. [21]	2.25	6.4×10^3	k-ω SST	11

2. MATERIAL AND METHODS

The present work numerically examines separated and reattaching flow over a two-dimensional backward-facing step (BFS) geometry. In the investigations, three eddy-viscosity based RANS turbulence models, e.g., Spalart-Allmaras, Realizable k-ε and SST k-ω, were evaluated by comparing their predictions with the experimental measurements of Li et al. [9].

2.1. Flow Geometry

A two-dimensional backward-facing step (BFS) geometry with a step height of h=25 mm, corresponding to an expansion ratio of H_o/H_i = 1.08, was employed. The Reynolds number of $Re_h = 9.6\times10^3$, based on the step height (h) and freestream velocity, U_∞, was selected to reproduce the experimental results obtained by Li et al. [9] to validate the numerical results of the present study. All geometrical details of the computational flow domain are given in Figure 1 [40].

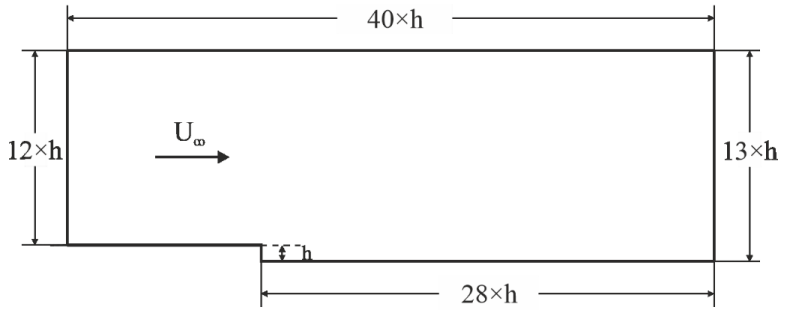


Figure 1. The geometrical details of the backward-facing step

2.2. The Governing Equations of the Flow

The governing equations for the flow over the backward-facing step (BFS) consist of the two-dimensional, incompressible continuity and Navier–Stokes equations, as presented in Equations (1) and (2).

$$\frac{\partial u_i}{\partial x_i} = 0 \tag{1}$$

$$\rho u_j \frac{\partial u_i}{\partial x_j} = -\frac{\partial P}{\partial x_i} + \mu \frac{\partial^2 u_i}{\partial x_j^2} + \rho g_i \tag{2}$$

Unsteady flow variables, density, ρ, velocities, u_j, are defined as follows

$$\rho = \bar{\rho} \text{ and } \rho' = 0, \quad u_j = \bar{u}_j + u_j', P = \bar{P} + P' \tag{3}$$

Putting the abovementioned definitions of the flow parameters, given in Equation (3), in the Navier-Stokes equation, given in Equation (2), gives the Reynolds equation as shown in Equation (4)

$$\bar{\rho}\bar{u}_j \left[\frac{\partial \bar{u}_i}{\partial x_j}\right] = -\frac{\partial \bar{P}}{\partial x_i} + \frac{\partial}{\partial x_j}\left[\mu \frac{\partial \bar{u}_i}{\partial x_j} - \overline{\rho u_i' u_j'}\right] + \bar{\rho} g_i \tag{4}$$

The Boussinesq approximation models the transport of turbulent velocity fluctuations analogously to molecular momentum transfer in an isotropic Newtonian fluid, as expressed in Equation (5).

$$\overline{\rho u_i' u_j'} = -\bar{\rho}\nu_t \left(\frac{\partial \bar{u}_j}{\partial x_i} + \frac{\partial \bar{u}_i}{\partial x_j}\right)$$

$$\bar{u}_j \frac{\partial \bar{u}_i}{\partial x_j} = -\frac{1}{\rho}\frac{\partial \bar{P}}{\partial x_i} + \frac{\partial}{\partial x_j}\left[(\nu + \nu_t)\left(\frac{\partial \bar{u}_j}{\partial x_i} + \frac{\partial \bar{u}_i}{\partial x_j}\right)\right] \tag{5}$$

2.3. Spalart-Allmaras Turbulence Mod

The Spalart–Allmaras turbulence model is a single-equation model that solves a transport equation for the kinematic eddy viscosity. It is generally applied to flows involving boundary layers subjected to adverse pressure gradients.

In this turbulence model, the kinematic eddy viscosity model is computed using Equation (6).

$$\nu_t = \tilde{\nu} f_{v1} \tag{6}$$

Here, the viscous damping function is $f_{v1} = \frac{\chi^3}{\chi^3 + C_{v1}^3}$ with $\chi \equiv \frac{\tilde{\nu}}{\nu}$ and C_{v1} is a model constant.

The transport equation for $\tilde{\nu}$ defined in this turbulence model is calculated using Equation (7).

$$\frac{\partial \tilde{\nu}}{\partial t} + u_j \frac{\partial \tilde{\nu}}{\partial x_j} = c_{b1}\tilde{S}\tilde{\nu} + \frac{1}{\sigma}\frac{\partial}{\partial x_i}\left\{(\nu + \tilde{\nu})\frac{\partial \tilde{\nu}}{\partial x_i}\right\} + \frac{c_{b2}}{\sigma}\left(\frac{\partial \tilde{\nu}}{\partial x_i}\right)^2 - c_{w1} f_w \left(\frac{\tilde{\nu}}{d}\right)^2 \tag{7}$$

In Equation (7), c_{b1}, c_{b2} and σ are constants and v is the molecular kinematic viscosity. Additionally, $\tilde{S}$ is calculated using Equation (8).

$$\tilde{S} \equiv S + \frac{\tilde{v}}{\kappa^2 + d^2} f_{v2} \tag{8}$$

Here, $f_{v2} = 1 - \frac{\chi}{1+\chi f_{v1}}$ and κ is constant while d denotes the distance from the wall. Moreover, S serves as a scalar indication of the deformation tensor which is based on the magnitude of the vorticity as $S \equiv \sqrt{2\Omega_{ij}\Omega_{ij}}$, where Ω_{ij} is the mean rate-of-rotation tensor defined by $\Omega_{ij} = \frac{1}{2}\left(\frac{\partial u_i}{\partial x_j} - \frac{\partial u_j}{\partial x_i}\right)$.

Finally, c_{w1} and f_w are calculated using $c_{w1} = \frac{c_{b1}}{\kappa^2} + \frac{(1+c_{b2})}{\sigma}$ and $f_w = g\left[\frac{1+c_{w3}^6}{g^6+c_{w3}^6}\right]^{1/6}$.

2.4. SST *k-ω* Turbulence Model

In 1993, Menter [41] introduced the SST *k–ω* turbulence model which aimed to combine the strengths of both *k-ε* and *k-ω* models. The SST *k–ω* model enhances predictive capability across varying flow regimes through a hybrid formulation that leverages the strengths of both *k–ω* and *k–ε* models.

In this turbulence model, the kinematic eddy viscosity is defined as given in Equation (9).

$$\nu_t = \frac{a_1 k}{max(a_1\omega; SF_2)} \tag{9}$$

Here, S is the invariant measure of the strain rate, i.e., S = $\sqrt{2S_{ij}S_{ij}}$ and F_2 is a second blending function defined by Equation (11).

$$F_2 = tanh\left\{\left\{max\left(\frac{2\sqrt{k}}{\beta_t^*\omega y_t}; \frac{500\nu}{y_t^2\omega}\right)\right\}^2\right\} \tag{10}$$

The transport equations for k and ω in the SST *k-ω* model are given in Equations (11) and (12) as follows.

$$\frac{Dk}{Dt} = \tilde{P}_k + \frac{\partial}{\partial x_i}\left[(\nu + \sigma_k\nu_t)\frac{\partial k}{\partial x_i}\right] - \beta_t^* k\omega \tag{11}$$

$$\frac{D\omega}{Dt} = \alpha S^2 + \frac{\partial}{\partial x_i}\left[(\nu + \sigma_\omega\nu_t)\frac{\partial \omega}{\partial x_i}\right] + 2(1-F_1)\sigma_{\omega 2}\frac{1}{\omega}\frac{\partial k}{\partial x_i}\frac{\partial \omega}{\partial x_i} - \beta_t\omega^2 \tag{12}$$

The blending function F_1 is defined as follows,

$$F_1 = tanh\left\{\left\{min\left[max\left(\frac{\sqrt{k}}{\beta_t^*\omega y_t}; \frac{500\nu}{y_t^2\omega}\right); \frac{4\rho\sigma_{\omega 2}k}{CD_{k\omega}y_t^2}\right]\right\}^4\right\} \tag{13}$$

with the following definition of the cross-diffusion term

$$CD_{k\omega} = max\left(2\rho\sigma_{\omega 2}\frac{1}{\omega}\frac{\partial k}{\partial x_i}\frac{\partial \omega}{\partial x_i};\ 10^{-10}\right) \tag{14}$$

and where y_t is the distance to the nearest wall. F_1 goes to zero away from the surface because of $1/y_t$ or $1/y_t^2$ dependency in all three terms in Equation (13). The blending function is defined such that it makes a smooth transition from k-ω at the wall to *k-ε* far from it.

The coefficients in the model are calculated from the blending function F_1 by using Equation (15).

$$\phi_t = F_1\phi_{t,1} + (1 - F_1)\phi_{t,2} \tag{15}$$

where subscript 1 represents the original coefficient of the k-ω model and subscript 2 represents the coefficients of the transformed k-ε model. The closure coefficients for the SST k-ω model are shown in Table 2.

Table 2. Coefficients of the SST k-ω model.

	β_t	σ_k	σ_ω	a_1	β_t^*	α
Set 1 ($\phi_{t,1}$)	0.0750	0.85	0.5	0.31	0.09	5/9
Set 2 ($\phi_{t,2}$)	0.0828	1.0	0.856			0.44

To prevent the build-up of turbulence in stagnation regions, Menter [41] proposed a production limiter which is defined as follows.

$$\tilde{P}_k = min(P_k; 10\beta_t^* k\omega) \tag{16}$$

Where

$$P_k = \nu_t \frac{\partial U_j}{\partial x_i}\left(\frac{\partial U_j}{\partial x_i} + \frac{\partial U_i}{\partial x_j}\right) \tag{17}$$

2.5. Realizable k-ε Turbulence Model

The Realizable k-ε model contains an alternative formulation for the turbulent viscosity that distinguishes it from standard k-ε turbulence model. In this turbulence model, the kinematic eddy viscosity is computed using Equation (18).

$$\nu_t = C_\mu \frac{k^2}{\varepsilon} \tag{18}$$

Here, $C_\mu = \frac{1}{A_0 + A_S\frac{kU^*}{\varepsilon}}$.

The transport equation of k and ε are given in Equations (19) and (20), respectively.

$$\frac{Dk}{Dt} = \nu_t S^2 + \frac{\partial}{\partial x_j}\left[\left(\nu + \frac{\nu_t}{\sigma_k}\right)\frac{\partial k}{\partial x_j}\right] - \varepsilon \tag{19}$$

$$\frac{D\varepsilon}{Dt} = C_1 S_\varepsilon + \frac{\partial}{\partial x_j}\left[\left(\nu + \frac{\nu_t}{\sigma_\varepsilon}\right)\frac{\partial \varepsilon}{\partial x_j}\right] - C_2\frac{\varepsilon^2}{k + \sqrt{\nu\varepsilon}} \tag{20}$$

Here, $C_1 = max\left[0.43, \frac{\eta}{\eta+5}\right]$, $\eta = S\frac{k}{\varepsilon}$ and $S = \sqrt{2S_{ij}S_{ij}}$, $S_{ij} = \frac{1}{2}\left(\frac{\partial u_j}{\partial x_i} + \frac{\partial u_i}{\partial x_j}\right)$.

In Equations (19) and (20), σ_k and σ_ε are the turbulent Prandtl numbers for k and ε, i.e., σ_k=1.0, σ_ε=1.2. Additionally, C_2 is a constant having a value of C_2=1.9.

The governing equations were discretized and solved with the aid of Ansys Fluent using a two-dimensional, steady-state RANS formulation for each turbulence model. Because no physical time integration was performed, a time-step size, temporal discretization scheme, total physical simulation time, and time step independence analysis, i.e., CFL number, are not applicable. Iterative convergence was considered achieved when the scaled residuals decreased below 10^{-5}. Pressure-velocity coupling was handled using the SIMPLEC algorithm. The least-squares cell-based method was used to compute the gradients of the flow variables, and the QUICK scheme was adopted for the discretization of the convective terms.

2.6. The Boundary Conditions of the Computational Flow Domain

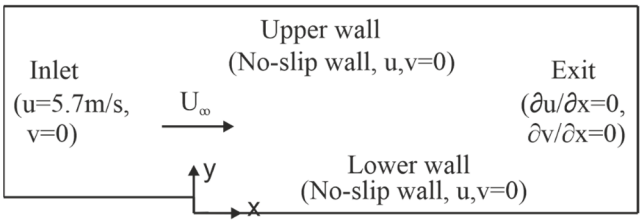


Figure 2. Boundary conditions of the computational flow domain

The boundary conditions of the computational domain are illustrated in Figure 2 and consist of inlet, outlet, and wall boundaries. A uniform velocity profile normal to the surface was specified at the inlet with a turbulence intensity of 1%, while a zero-gradient condition was applied at the outlet and no-slip boundary conditions were used on all walls.

2.7. Details of the Computational Mesh and Its Verification

Three different meshes were created to identify the most appropriate mesh that would not influence the numerical results. In the mesh independence study, the mesh with the fewest nodes was designated as the coarse mesh, whereas the one with the greatest number of nodes was designated as the fine mesh. The pressure coefficient, C_p, distribution was selected as the criterion for evaluating mesh adequacy. Figure 3 presents the $C_p$distribution along the lower surface of the channel downstream of the step for three turbulence models, obtained using the three different meshes.

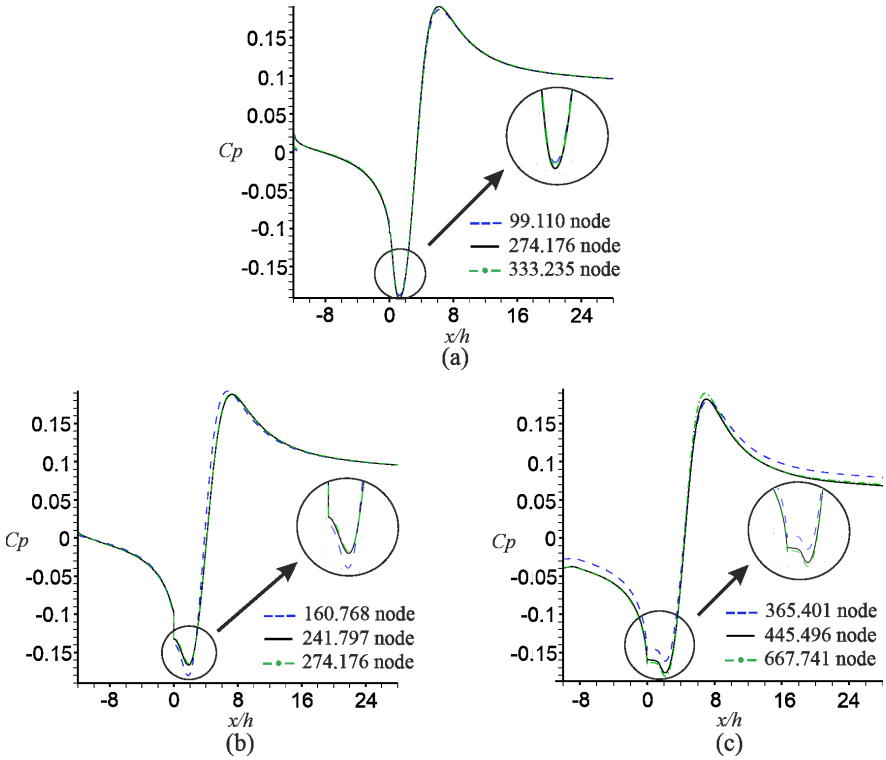


Figure 3. Pressure coefficient, C_p, results of three meshes for a. Spalart-Allmaras model, b. Realizable k-ε model c. SST k-ω model

Figure 3 illustrates that the results obtained from the medium and fine meshes for all turbulence models were in close agreement. Therefore, the medium mesh was selected for the present study, as it provides accurate results while reducing computational cost. Furthermore, Table 3 summarizes the maximum values of the dimensionless wall thickness, y^+, for the meshes used in the mesh independence study, along with their corresponding reattachment results.

Table 3. The maximum values of the dimensionless wall thickness, y^+, for the meshes used in the mesh independence study, along with their corresponding reattachment results

Turbulence model	Total number of nodes	y^+	X_r/h
Spalart-Allmaras	99.110	40	4.76
	274.176	44	4.60
	333.235	65	4.90
Realizable *k-ε*	160.768	57	4.90
	241.797	40	5.32
	274.176	40	5.29
SST *k-ω*	365.401	1.58	5.50
	445.496	0.94	5.80
	667.741	0.94	5.76

The y^+results presented in Table 3 indicate that the boundary layer meshes employed for the simulations possessed the required characteristics for the turbulence models used. Additionally, Figure 4 illustrates the mesh configurations, both with and without boundary layer meshes along the channel walls.

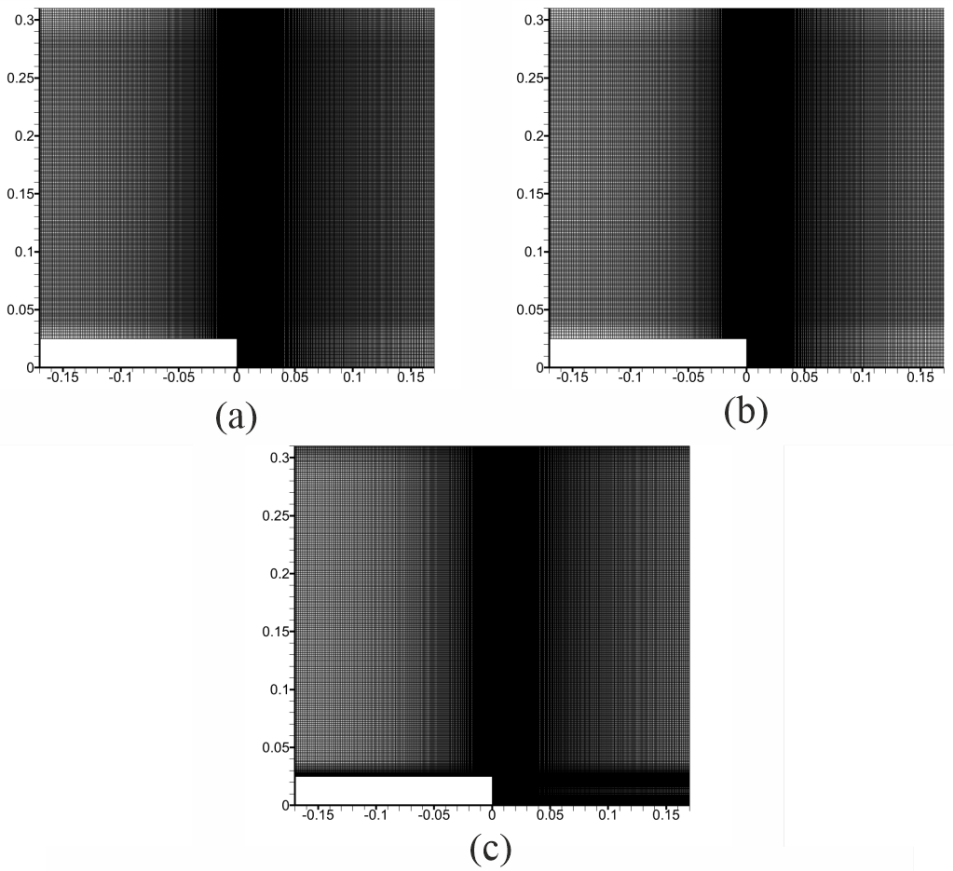


Figure 4. Computational meshes of the study using (a) the Spalart Allmaras model, (b) the Realizable *k-ε* model and (c) the SST *k-ω* model

3. RESULTS AND DISCUSSION

The flow over a backward-facing step (BFS) is a canonical benchmark problem for separated and reattaching flows [42]. Thus, the present study employed the BFS configuration with an expansion ratio of H_o/H_i =1.08 to investigate the performance of three different RANS-based turbulence models, which are Realizable *k-ε*, Spalart-Allmaras and SST *k- ω* respectively at the Reynolds number of $Re_h = 9.6 \times 10^3$.

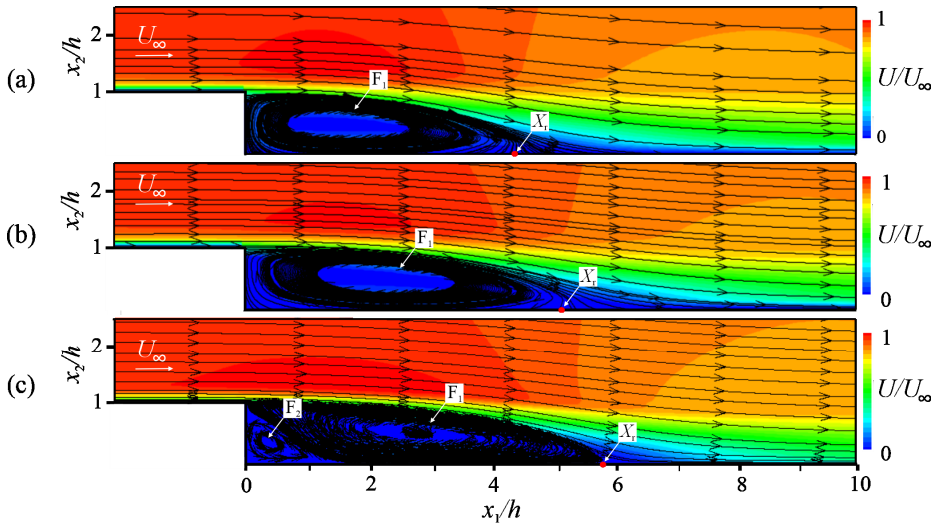


Figure 5. Streamlines, ψ, and velocity magnitude $U/U_\infty = \sqrt{u^2 + v^2}/U_\infty$, contours obtained by using (a) Spalart-Allmaras (b) Realizable k-ε and (c) SST k- ω turbulence models

Comparison of streamlines, ψ, and velocity magnitude, U/U_∞, contours are given Figure 5. The location of the reattachment point is shown with a red dot on each figure. The recirculation region formed due to flow separation at the top corner of the step was successfully captured by all three turbulence models. However, the recirculation regions of BFS flows showed differences for all three turbulence models. For instance, a secondary small recirculation region, F_2, was captured as the result of SST k-ω turbulence model whereas there are no secondary recirculation regions in the Spalart-Allmaras and Realizable k-ε turbulence models. The secondary small recirculation region (e.g., focus F_2) forming near the lower step corner was also seen in the experimental study of Li et al. [9]. The reattachment lengths were found as X_r/h=5.8, 5.32, and 4.6 by the SST k-ω, the Realizable k-ε, and the Spalart-Allmaras models, respectively, which were given 38.1%, 26.7%, and 9.52% differences when compared to the experimental result of Li et al. [9]. Thus, the result of Spalart-Allmaras provided the best estimation among the turbulence models that were employed in the present study, as in the study of Wilcox [15].

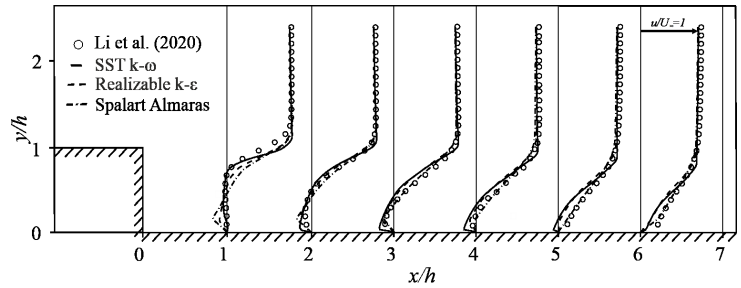


Figure 6. The comparison of the streamwise velocity component of different turbulence models normalized with the free stream velocity, u/U_∞, with the experimental results

The comparison of the streamwise velocity component profiles of different turbulence models normalized with the free-stream velocity, u/U_∞, as shown in Figure 6, exhibited good agreement with the experimental results of Li et al. [9] except at locations close to the base of BFS and the shear layer. In the recirculation area (i.e., $x/h \leq 5$), the streamwise velocity component results of turbulence models showed negative values at varying maximum magnitudes. The maximum difference of 191 % with the experimental results of Li et al. [9] was in the results of Spalart-Allmaras at x/h = 1. On the other hand, the velocity profiles of SST k-ω and Li et al. [9] at locations between $1 \leq x/h \leq 3$, showed good agreement, with a maximum difference of 5%. Besides, in the shear layer region, the velocity profiles obtained using the SST k-ω model showed a maximum difference of 42% at $x/h = 1$compared to the experimental results of Li et al. [9]. Moreover, at the locations after the reattachment point (i.e., at $x/h \geq 6$), at which the boundary layer redeveloped due to the wall effects, the maximum difference of 61% with the experimental results of Li et al. [9] was in the results of SST k-ω. Overall, the results showed that the Spalart–Allmaras model was in good agreement

with the findings of Li et al. [9] in both the shear layer and downstream of the reattachment point, whereas the SST k-ω model exhibited better agreement in the recirculation region. On the other hand, the results of the Realizable k-ε were worse than the results of other turbulence models.

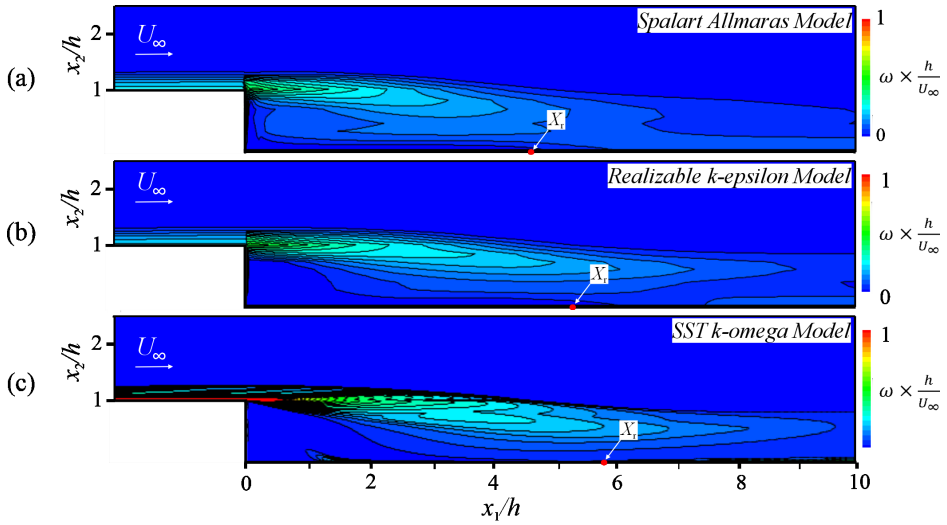


Figure 7. Vorticity, $\omega \times \frac{h}{U_\infty}$, contours obtained by using three different turbulence models

The comparison of the vorticity, $\omega \times \frac{h}{U_\infty}$, results obtained by using different turbulence models are given in Figure 7. Despite the use of different turbulence models, the vorticity contours exhibited a consistent overall structure; high vorticity regions were primarily located along the upper wall boundary layer and within the shear layer originating from the step corner. However, in line with the findings about the reattachment length given above, the estimation of the vorticity magnitude by the SST k–ω turbulence model gave the maximum amount at around the upper corner of the step when compared to the other turbulence models, i.e., the Realizable k-ε and Spalart–Allmaras turbulence models. The higher vorticity concentrations observed within the shear layer indicate stronger shear gradients and more intense mixing, which enhance the momentum transfer between the free stream and the recirculation zone. Furthermore, both the Realizable k–ε and SST k–ω models exhibited vorticity contours extending further downstream than those predicted by the Spalart–Allmaras model, indicating increased turbulence intensity and shear layer instability, which may contribute to a delayed reattachment.

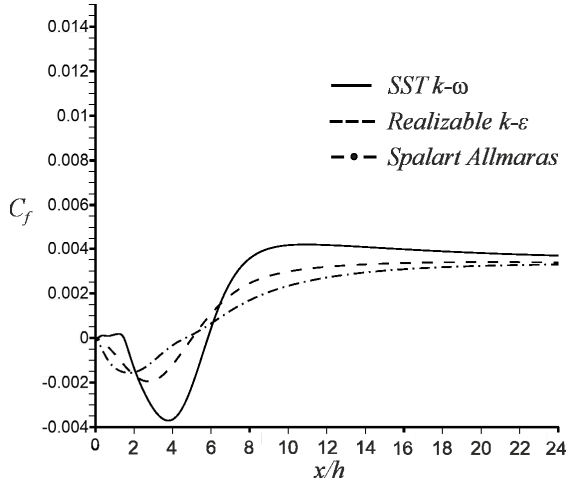


Figure 8. Skin friction coefficient, C_f, profile on the lower wall of the channel downstream of the backward-facing step (BFS)

Figure 8 presents a comparison of the skin friction coefficient, C_f on the lower wall of the channel obtained by using three different turbulence models. The results given in Figure 8 show that the skin friction

coefficient, C_f, attains negative values due to reversed flow in the recirculation region downstream of the BFS. The C_f values continue to decrease, reaching a minimum within the recirculation zone, and subsequently recover in the downstream direction. Similar trends for the C_f were seen in the results given in the previous studies [12, 28, 43]. Although the trends followed by the C_f results of all turbulence models were the same, their absolute maximums at extreme points were not the same. For example, the absolute maximums of C_f results of SST k-ω turbulence model were greater than the results of Realizable k-ε and Spalart-Allmaras turbulence models, both in the recirculation region and after the reattachment point. Additionally, the C_f distribution along the lower wall can be used to determine the reattachment point, as the skin friction coefficient becomes zero at this location [44]. Thus, as shown in Figure 8, the point at which the $C_f = 0$ corresponds to x/h = 4.6, 5.32, and 5.8 for the results of Spalart-Allmaras, Realizable k-ε and SST k-ω turbulence models, respectively, which are the same values of the reattachment points reported as above sections.

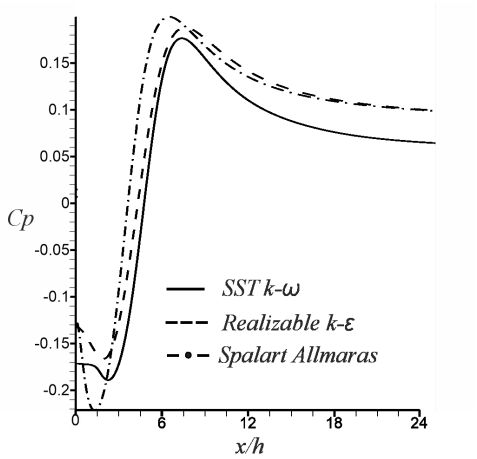


Figure 9. The profile of the pressure coefficient, C_p, on the lower wall of the flow over the BFS

A comparison of the pressure coefficient, C_p, results on the lower wall of the channel for different turbulence models is presented in Figure 9. The negative pressure coefficient observed near the step indicates the presence of a low-pressure region due to flow separation. The pressure coefficient results are in good agreement with trends reported in the literature [36,45]. Although C_p showed a similar decrease in the lower wall near the step for Realizable k-ε and Spalart-Allmaras models, the decrease in C_p almost stopped between 0<x<0.05 due to the secondary circulation region in the lower wall near the step for the SST k-ω turbulence model. Then, C_p gradually increased again in the downward flow. Among the three models, the C_p increased more sharply in the Spalart-Allmaras model. While the Realizable k-ε and Spalart Allmaras models show good agreement at the inlet, differences appear after the step and persist until reattachment.

4. CONCLUSIONS

This study compared the predictive performance of the Spalart-Allmaras, Realizable k-ε and SST k-ω turbulence models for a two-dimensional backward-facing step (BFS) flow at Re_h=9.6×10^3 and H_o/H_i=1.08. In the prediction of the reattachment length, the Spalart-Allmaras model produced the smallest error, i.e., 9.52%, followed by the Realizable k-ε model, i.e., 26.7%, and the SST k-ω model, i.e., 38.1% relative to the experimental results reported by Li et al. [9].

On the other hand, when comparing the local-flow results, the performance of the turbulence models depends on the region and the flow quantity considered. The Spalart-Allmaras model agreed more closely with the experimental velocity profiles in the shear layer and downstream of the reattachment location, whereas the SST k-ω model reproduced the velocity distribution within the recirculation region with a maximum difference of 5% and captured the secondary recirculation structure observed experimentally. On the other hand, the SST k-ω model produced the highest vorticity levels near the upper step corner. These findings show that reattachment length alone is not sufficient to establish the overall superiority of a turbulence model for separated and reattaching flows.

Nevertheless, the reported results of turbulence models should be interpreted only for the investigated condition and should not be generalized to a broad Reynolds-number range because the comparison is limited to a single Reynolds number and expansion ratio corresponding to the selected experimental benchmark. Future work might examine several Reynolds numbers, expansion ratios and inlet boundary layer conditions together with three-dimensional investigation.

In conclusion, under the present flow and geometrical conditions, the Spalart-Allmaras model is recommended when reattachment length and post-reattachment behaviour are the main quantities of interest, whereas the SST k-ω model may be preferable when the internal structure of the recirculation region is the primary focus.

5. REFERENCES

1. Uruba, V., Jonas, P. & Mazur, O. (2007). Control of a channel flow behind a backward-facing step by suction/blowing. *International Journal of Heat and Fluid Flow*, *28*(4), 665-672.
2. Geropp, D. & Odenthal, H.-J. (2000). Drag reduction of motor vehicles by active flow control using the Coanda effect. *Experiments in Fluids*, *28*(1), 74-85.
3. Koca, F. ve Gürlek, C., (2023). Dikdörtgensel engellerin dairesel oluklu bir kanalın ısıl-hidrolik özellikleri üzerindeki etkilerinin sayısal olarak incelenmesi. *Çukurova Üniversitesi, Mühendislik Fakültesi Dergisi, 38*(3), 661-670.
4. Alnak, D.E. ve Karabulut, K. (2021). Jet giriş genişliğinin ısı transferi ve akış yapısına olan etkisinin araştırılması. *Çukurova Üniversitesi Mühendislik Fakültesi Dergisi*, 36(2), 331-345.
5. Lee, T. & Mateescu, D. (1998). Experimental and numerical investigation of 2-D backward-facing step flow. *Journal of Fluids and Structures*, *12*(6), 703-716.
6. Cuvier, C., Foucaut, J.-M., Braud, C. & Stanislas, M. (2013). PIV characterisation of a flow separation induced by a 22° flap. In *International Symposium on Turbulence and Shear Flow Phenomena (TSFP-8)*, 28-30 August 2013, Poitiers, France.
7. Eaton, J.K. & Johnston, J.P. (1981). A review of research on subsonic turbulent flow reattachment. *AIAA Journal*, *19*(9), 1093-1100.
8. Chen, L., Asai, K., Nonomura, T., Xi, G. & Liu, T. (2018). A review of backward-facing step (BFS) flow mechanisms, heat transfer and control. *Thermal Science and Engineering Progress*, *6*, 194-216.
9. Li, Z., Zhang, D., Liu, Y., Wu, C. & Gao, N. (2020). Effect of periodic perturbations on the turbulence statistics in a backward-facing step flow. *Physics of Fluids*, *32*, 075116.
10. Tihon, J., Legrand, J. & Legentilhomme, P. (2001). Near-wall investigation of backward-facing step flows. *Experiments in Fluids*, *31*, 484-493.
11. Al-Jelawy, H., Kaczmarczyk, S., AlKhafaji, D., Mirhadizadeh, S., Lewis, R. & Cross, M. (2016). A computational investigation of a turbulent flow over a backward facing step with OpenFOAM. *2016 9th International Conference on Developments in eSystems Engineering (DeSE)*, Liverpool, UK, 301-307.
12. Pedersen, O., Fleit, G., Pummer, E., Tullis, B.P. & Rüther, N. (2018). Reynolds-averaged Navier-Stokes modeling of submerged ogee weirs. *Journal of Irrigation and Drainage Engineering, 144*(1), 04017059.
13. Karabulut, K. & Alnak, Y. (2023). Analysis of heat transfer and flow structure from distinct model facets depending on the number of jet flows in channel. *Çukurova University Journal of the Faculty of Engineering, 38*(1), 49-60.
14. Schafer, F, Breuer, M & Durst, F. (2009). The dynamics of the transitional flow over a backward-facing step. *Journal of Fluid Mechanics*, *623*, 85-119.
15. Wilcox, D.C. (2006). *Turbulence modeling for CFD* (3rd ed.). DCW Industries.
16. Driver, D.M. & Seegmiller, H.L. (1985). Features of a reattaching turbulent shear layer in divergent channel flow. *AIAA Journal*, *23*(2), 163-171.
17. Gatski, T.B., Hussaini, M.Y. & Lumley, J.L. (Eds.) (1996). *Simulation and modeling of turbulent flows.* Oxford University Press.
18. Bredberg, J. & Davidson, L. (2004). Low-Reynolds number turbulence models: An approach for reducing mesh sensitivity. *Journal of Fluids Engineering*, *126*(1), 14-21.
19. Thangam, S. & Speziale, C.G. (1992). Turbulent flow past a backward-facing step: A critical evaluation of two-equation models. *AIAA Journal*, *30*(5), 1314-1320.
20. Shih, T.-H., Liou, W.W., Shabbir, A., Yang, Z. & Zhu, J. (1995). A new $k-\varepsilon$ eddy viscosity model for high Reynolds number turbulent flows. *Computers & Fluids*, *24*(3), 227-238.

21. Munters, W., Koloszar, L. & Planquart, P. (2022). Numerical simulation of a confined backward-facing step flow using hybrid turbulence models in OpenFOAM. In: *Conference on Fluid Flow (CMFF'22)*, Budapest, Hungary, 30August - 2 September 2022.

22. Le, H., Moin, P. & Kim, J. (1997). Direct numerical simulation of turbulent flow over a backward-facing step. *Journal of Fluid Mechanics*, *330*, 349-374.

23. Kaiktsis, L., Karniadakis, G.E. & Orszag, S.A. (1991). Onset of three-dimensionality, equilibria, and early transition in flow over a backward-facing step. *Journal of Fluid Mechanics*, *231*, 501-528.

24. Kaiktsis, L., Karniadakis, G.E. & Orszag, S.A. (1996). Unsteadiness and convective instabilities in two-dimensional flow over a backward-facing step. *Journal of Fluid Mechanics*, *321*, 157-187.

25. Neto, A.S., Grand, D., Métais, O. & Lesieur, M. (1993). A numerical investigation of the coherent vortices in turbulence behind a backward-facing step. *Journal of Fluid Mechanics*, *256*, *1-25*.

26. Zontul, H. ve Şahin, B. (2020). Zamanla sinüzoidal olarak değişen manyetik alan şiddetinin ters basamak geometrisinde akış ayrılması ve ısı transferine etkisi. *Çukurova University Journal of the Faculty of Engineering and Architecture*, *35*(2), 413-424.

27. Addad, Y., Laurence, D., Talotte, C. & Jacob, M.C. (2003). Large eddy simulation of a forward–backward-facing step for acoustic source identification. *International Journal of Heat and Fluid Flow 24*(4), 562-571.

28. Khuwaranyu, K. & Putivisutisak, S. (2009). Combined low-Reynolds-number k–ω model with length scale correction term for recirculating flows. *Journal of Engineering and Technology Research*, *1*(8), 171-180.

29. Kang, S. & Choi, H. (2002). Suboptimal feedback control of turbulent flow over a backward-facing step. *J. Fluid Mech.*, *463*, 201-227.

30. Okada, K., Nonomura, T., Fujii, K. & Miyaji, K. (2012). Computational analysis of vortex structures induced by a synthetic jet to control separated flows. *International Journal of Flow Control*, *4*, 47-66.

31. Avancha, R.V.R. & Pletcher, R.H. (2002). Large eddy simulation of the turbulent flow past a backward-facing step with heat transfer and property variations. *International Journal of Heat and Fluid Flow*, *23*, 601-614.

32. Dejoan, A. & Leschziner, M.A. (2004). Large eddy simulation of periodically perturbed separated flow over a backward-facing step. *International Journal of Heat and Fluid Flow*, *25*, 581-592.

33. Rhee, G.H. & Sung, H.J. (2000). Numerical prediction of locally forced turbulent separated and reattaching flow. *Fluid Dynamics Research*, *26*(6), 421-436.

34. Mehrez, Z., Bouterra, M., Elcafsi, A., Belghith, A. & Le Quéré, P. (2010). Active control of flow behind a backward facing step by using a periodic perturbation. *ARPN Journal of Engineering and Applied Sciences*, *5*(2), 21-29.

35. Choi, S.W. & Kim, H.S. (2020). Predicting turbulent flows in butterfly valves with the nonlinear eddy viscosity and explicit algebraic Reynolds stress models. *Phys. Fluids*, *32*, 085105.

36. Kumar, A.S., Singh, A. & Thiagarajan, K.B. (2020). Simulation of backward facing step flow using OpenFOAM. *AIP Conference Proceedings, 2204*(1), 030002.

37. Barri, M. & Andersson, H.I. (2010). Turbulent flow over a backward-facing step. Part 1. Effects of anti-cyclonic system rotation. *Journal of Fluid Mechanics*, *665*, 382-417.

38. Louda, P., Příhoda, J., Kozel, K. & Svácek, P. (2013). Numerical simulation of flows over 2D and 3D backward-facing inclined steps. *International Journal of Heat and Fluid Flow*, *43*, 268-276.

39. Juste, G.L., Fajardo, P. & Guijarro, A. (2016). Assessment of secondary bubble formation on a backward-facing step geometry. *Phys. Fluids*, *28*, 074106.

40. Erkoc, A.R. (2025). Control of the flow downstream of a backward-facing step. *Master's thesis*. Adana Alparslan Türkeş Science and Technology University, Graduate Education Institute, Department of Mechanical Engineering, Division of Mechanical Engineering, 891441.

41. Menter, F.R. (1993). Zonal two equation k-ω turbulence models for aerodynamic flows. *AIAA 23rd Fluid Dynamics Plasma dynamics, and Lasers Conference*, 6-9 July 1993 Orlando, FL, U.S.A.

42. Abu-Nada, E. (2008). Application of nanofluids for heat transfer enhancement of separated flow encountered in a backward facing step. *International Journal of Heat and Fluid Flow*, *29*(1), 242-249.

43. Rani, H.P., Sheu, T.W.H. & Tsai, E.S.F. (2007). Eddy structures in a transitional backward-facing step flow. *J. Fluid Mech.*, *588*, 43-58.

44. Hu, R., Wang, L. & Fu, S. (2020). Modelling and numerical simulation for flow control. In: Qin, N., Periaux, J., Bugeda, G. (eds), *Advances in Effective Flow Separation Control for Aircraft Drag Reduction (Computational Methods in Applied Sciences, 52*, 317-338. Springer, Cham.

45. Nakagawa, H. & Nezu, I. (1987). Experimental investigation on turbulent structure of backward-facing step flow in an open channel. *Journal of Hydraulic Research*, *25*(1), 67-88.